

## ARTICLE OPEN



# An additively manufactured magnesium-aluminium alloy withstands seawater corrosion

Zhuoran Zeng<sup>1</sup>✉, Sanjay Choudhary<sup>2</sup>, Marco Esmaily<sup>3,4</sup>, Felix Benn<sup>5,6</sup>, Thomas Derra<sup>5</sup>, Yvonne Hora<sup>7,8</sup>, Alexander Kopp<sup>5</sup>, Antoine Allanore<sup>3</sup> and Nick Birbilis<sup>1</sup>✉

Magnesium, the lightest structural metal, has inherently poor corrosion resistance. In this study, we developed a magnesium-aluminium Mg-10.6Al-0.6Zn-0.3Mn alloy, additively manufactured by laser powder bed fusion. We reveal that this alloy has a record low degradation rate amongst all magnesium alloys in practically relevant corrosive solutions, and it even withstands seawater corrosion. As tested by a number of methods, the alloy shows even more enhanced passivation with longer immersion periods. The alloy surface following immersion maintained a nearly corrosion-free appearance and was determined to have a thin aluminium-containing surface film, due to surface enrichment of aluminium from the supersaturated matrix. Aluminium enrichment near the sample surface was also observed when the sample is immersed in phosphoric acid or exposed to atmosphere at room temperature. This study demonstrates the prospects for additively manufactured ultra-lightweight magnesium structure with outstanding corrosion resistance.

npj Materials Degradation (2022)6:32; <https://doi.org/10.1038/s41529-022-00241-5>

## INTRODUCTION

The density of magnesium (Mg) is  $1.74 \text{ g cm}^{-3}$  at  $20^\circ\text{C}$ , approximately two-thirds that of aluminium (Al) and a quarter that of steel. This makes Mg alloys important for a wide range of applications including transportation, aerospace, and consumer goods<sup>1,2</sup>. The volumetric density of Mg components can be further decreased through the manufacturing of products via laser powder-bed fusion (LPBF). The method enables design capabilities not achievable with traditional manufacturing, making this class of lightest engineering alloys even lighter by topology optimisation and the use of free space as a design variable. This is significant for aircraft, aerospace, and transportation industries, and biodegradable implant and electrode applications<sup>3–5</sup>. As noted by several recent works<sup>6–15</sup>, the LPBF method is routinely and reproducibly utilized to safely manufacture Mg-alloys of diverse composition. The outstanding mechanical properties have been demonstrated as achievable from the LPBF of Mg alloys. For LPBF-prepared WE43 (Mg-4Y-3RE-0.4Zr), a yield strength of  $\sim 300 \text{ MPa}$  and elongation of  $\sim 12.2\%$  were demonstrated<sup>15</sup>. These values are considerably higher than the properties of extruded WE43 in the T6 condition ( $160 \text{ MPa}$  yield strength and  $6\%$  in elongation)<sup>16</sup>. However, open questions remain as to (i) can the LPBF process be exploited to study alloy compositions unique to LPBF?; and (ii) can LPBF-prepared Mg-alloys overcome the longstanding concern of a fast degradation rate of Mg alloys? Apart from a few exceptions<sup>17</sup>, the majority of Mg-alloys used industrially have a rapid corrosion rate<sup>18</sup>, and the oxide/hydroxide surface layer is soluble in most aqueous environments and thus does not offer suitable corrosion protection; as outlined in detail elsewhere<sup>19</sup>.

Of the efforts made to improve the corrosion resistance of Mg-alloys, in the context of inherent corrosion resistance as opposed to coatings or platings, the explored methods include refining

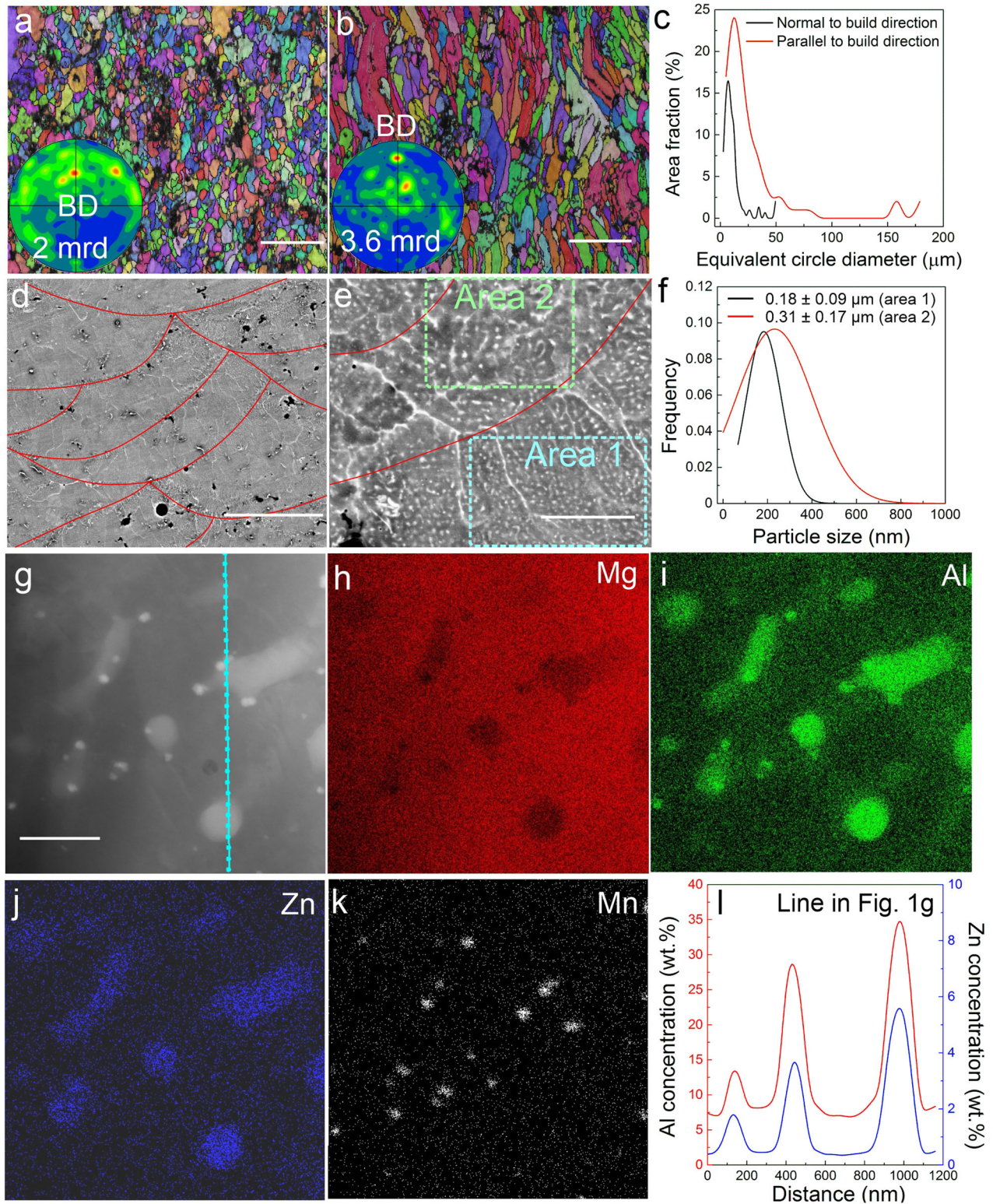
microstructure to minimize localised corrosion<sup>20–22</sup> and tailoring alloy compositions<sup>17,23</sup>. To date for Mg-alloy compositions explored that have non-LPBF-prepared alloy counterparts—it was determined that the LPBF-prepared alloys had faster corrosion rates<sup>24,25</sup>. Such a finding has also been determined for other LPBF-prepared alloys when compared to wrought counterparts<sup>26,27</sup>. However, as has been noted as an advantage of LPBF manufacturing, the high local temperatures and rapid solidification rates allow opportunities to produce alloy compositions that are otherwise difficult to achieve by conventional casting. In such a context—atypical compositions for LPBF may be explored. In this study, an Mg-10.6Al-0.6Zn-0.3Mn wt.% (AZ111) alloy was produced by LPBF, which is a higher Al-containing alloy than the well-known Mg-alloy AZ91. In contrast to previous reports over the past century of rapid corrosion for Mg alloys, this work demonstrated that the lowest corrosion rate reported for any Mg-alloy to date was achieved for the LPBF-prepared alloy studied herein. The LPBF-AZ111 alloy revealed limited corrosion in appearance even with immersion in seawater and NaCl electrolyte for 14 days. The purpose of this paper is to report the exceptional corrosion resistance of the additively manufactured alloy class and discuss the underlying degradation/passivation mechanism.

## RESULTS

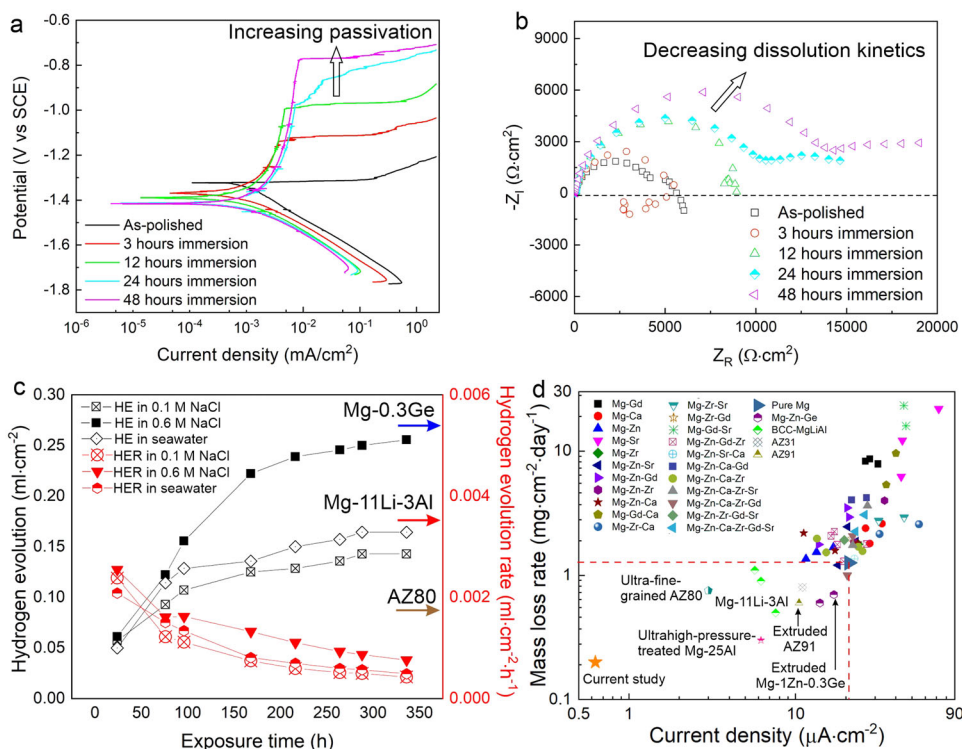
### Microstructure of LPBF-AZ111 alloy

Figure 1 shows the microstructure of LPBF-fabricated AZ111 alloy. Viewed along the build direction (BD), grains had an equiaxed shape with an average grain size of  $\sim 10 \mu\text{m}$  (Fig. 1a). Perpendicular to the BD, the grain morphology reveals elongation with averaged equivalent circle diameter of  $28 \mu\text{m}$  (Fig. 1b, c). Irrespective of which surface was observed, the grains had a

<sup>1</sup>College of Engineering and Computer Science, Australian National University, ACT, Acton 2601, Australia. <sup>2</sup>Department of Materials Science and Engineering, Monash University, Clayton, VIC 3800, Australia. <sup>3</sup>Department of Materials Science and Engineering, Massachusetts Institute of Technology, Cambridge, MA 02139, USA. <sup>4</sup>Volvo Materials Technology Laboratory, Volvo Group, Lundby, Gothenburg 417 15, Sweden. <sup>5</sup>Meotec GmbH, Philipsstr. 8, Aachen, Germany. <sup>6</sup>School of Mechanical and Aerospace Engineering, Queen's University Belfast, Belfast BT7 1NN, UK. <sup>7</sup>Monash X-ray Platform, Monash University, Clayton, VIC 3800, Australia. <sup>8</sup>Department of Chemical and Biological Engineering, Monash University, Clayton, VIC 3800, Australia. ✉email: [zhuoran.zeng@anu.edu.au](mailto:zhuoran.zeng@anu.edu.au); [nick.birbilis@anu.edu.au](mailto:nick.birbilis@anu.edu.au)



**Fig. 1 Electron microscopy characterisation.** EBSD orientation map and corresponding (0001) pole figures of sample surfaces that are **a** normal and **b** parallel to the build direction. **c** Histogram showing the distribution of grain size in **a** and **b**. Scanning electron microscopy (SEM) backscattered electron images (BSE) showing **(d)** melt pool at low magnification and **(e)** ultra-fine particles dispersed within the melt pool and coarser particles between melt pools and grain boundaries. **f** Particle size distribution in Area 1 and Area 2 shown in **e**. **g–k** High-angle annular dark-field scanning transmission electron microscopy (HAADF-STEM) and corresponding STEM energy-dispersive X-ray spectroscopy (EDXS) mapping showing ultra-fine particles and elemental distribution. **l** Profile showing the concentration of Al and Zn along the line in **g**. Scale bars in **a**, **b**, **d**, **e**, and **g** indicate 50  $\mu\text{m}$ , 50  $\mu\text{m}$ , 50  $\mu\text{m}$ , 5  $\mu\text{m}$ , and 300 nm, respectively.



**Fig. 2** Electrochemical chemical and immersion test. **a** potentiodynamic polarisation curves, **b** electrochemical impedance spectroscopy Nyquist plots of AZ111 alloy after immersion up to 48 h in 0.1 M NaCl electrolyte, **c** Accumulated hydrogen evolution (HE), and hydrogen evolution rate (HER) of the sample after 14 days immersion in 0.1 M and 0.6 M NaCl electrolyte, and seawater, **d** Comparison of the mass-loss rate and corrosion current density of AZ111 alloy with some typical Mg alloys in 0.1 M NaCl electrolyte<sup>17,20,30–33</sup>. Solid arrows in (c) show the hydrogen evolution rate of several corrosion-resistant Mg alloy, Mg-0.3Ge<sup>23</sup>, Mg-11Li-3Al<sup>17</sup>, and ultra-fine-grained AZ80 alloys<sup>20</sup>. Red dashed lines in (d) show mass-loss rate and corrosion current density of pure Mg as a benchmark<sup>31</sup>.

randomised texture, only 2.0 mrd along the BD and 3.6 mrd perpendicular to the BD. The melt pools were in the size range of  $\sim 100\ \mu\text{m}$  in width and  $\sim 20\text{--}50\ \mu\text{m}$  in height (Fig. 1d). The melt pool boundaries were enriched in dendritic intermetallics. Within each grain, there was a high number density of spherical particles, as shown in Area 1 (Fig. 1e). The diameter of these spherical particles was  $0.18 \pm 0.09\ \mu\text{m}$ , which was smaller than the equivalent circle diameter of dendritic particles ( $0.31 \pm 0.17\ \mu\text{m}$ ) near the melt pool boundary (highlighted in Area 2 in Fig. 1f).

The ultra-fine particles were further examined at higher magnification (Fig. 1g–k). Two types of particles were observed. One type was the larger spherical and elliptical-type particles with enriched Al and Zn ( $\sim 100\text{--}300\ \text{nm}$  in diameter). The other type was smaller Al-Mn nano-particles with a size up to  $\sim 20\ \text{nm}$  in diameter. In the alloy matrix, the concentration of Al and Zn was semi-quantitatively identified  $\sim 7.5\ \text{wt.}\%$  and  $\sim 0.5\ \text{wt.}\%$ , respectively (Fig. 1l). For the Mg-Al-Zn particles, the concentration of Al and Zn was higher. The method X-ray diffraction (XRD) revealed the  $\alpha\text{-Mg}$  and  $\beta\text{-phase}$  in the LPBF-AZ111 alloy (Supplementary Fig. 1), and therefore such Mg-Al-Zn particles were identified to be a Zn-containing variant of the  $\beta\text{-phase}$ , i.e.,  $\text{Mg}_{17}(\text{Al}, \text{Zn})_{12}$ .

### Corrosion behaviour

When tested in the as-ground state immediately following immersion in 0.1 M NaCl, no passivation was observed in the polarisation curve (Fig. 2a). The sample corrosion current density  $i_{\text{corr}}$  was  $2.8\ \mu\text{A}\cdot\text{cm}^{-2}$  with a corrosion potential,  $E_{\text{corr}}$ , of  $-1.33\ \text{V}_{\text{SCE}}$ . However, with an increase in the immersion time, the dynamic emergence of significant passivation was observed from inspection of the anodic branch of polarisation curves. The cathodic kinetics (representing the water reduction reaction) measured upon AZ111 as a function of immersion time revealed a

notable decrease with immersion time. The electrochemically determined corrosion rate ( $i_{\text{corr}}$ ) was  $0.63\ \mu\text{A}\cdot\text{cm}^{-2}$  following immersion in 0.1 M NaCl for 48 h. The potentiodynamic polarisation tests for each immersion time were conducted on a unique sample, with the immersion time representing the duration of open-circuit conditioning. In order to validate the reproducibility of  $i_{\text{corr}}$  measurements, two samples from different as-built blocks ( $12\ \text{mm} \times 10\ \text{mm} \times 10\ \text{mm}$ ) were also tested in 0.1 NaCl up to 96 h. The exposure surface of both samples was perpendicular to the build direction. Sample 1 was taken at a height of around  $\sim 3\ \text{mm}$  (close to the bottom of the specimen) and sample 2 was taken from a height of around  $9\ \text{mm}$  (close to the top of the specimen), with both samples revealing very similar results from polarisation testing (Supplementary Fig. 2).

Consistent with results from the potentiodynamic polarisation testing, independent testing using electrochemical impedance spectroscopy (EIS) also revealed an increased impedance with the increased immersion duration. From the Nyquist plots shown (Fig. 2b), the charge transfer resistance at low frequency was increased from  $\sim 5600\ \Omega\cdot\text{cm}^2$  in the as-ground state to  $>15,000\ \Omega\cdot\text{cm}^2$  after 48 h immersion. Furthermore, the form of the Nyquist plots for 24 and 48 h immersion reveal a diffusional process that is notionally concomitant with the presence of a protective surface layer (for uncoated metals or alloys)—where the imaginary component— $Z_i(\omega)$  of the Nyquist plot is always  $>0$  (often modelled by a Warburg element)<sup>28</sup>.

Aside from electrochemical testing, immersion testing and hydrogen collection were carried out upon independent specimens. During immersion in 0.1 M and 0.6 M NaCl (equivalent to  $\text{Cl}^-$  concentration in seawater) and real seawater, the volume of generated hydrogen (as an index to corrosion rate) was extremely low (Fig. 2c). Moreover, longer immersion times revealed a lower

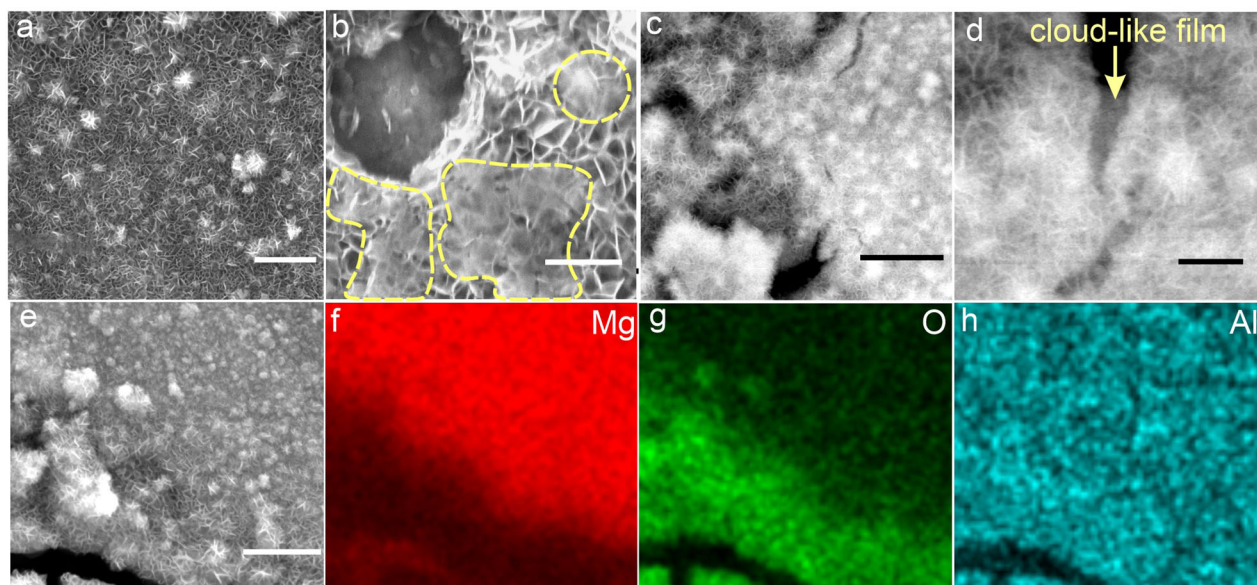


**Fig. 3** Electron microscopy observation of alloy surface after immersion in 0.1 M NaCl. **a, b** SE-SEM image of surface without localised corrosion and **c, d** BSE-SEM image of surface area with localised corrosion, and **e–h** SE and corresponding EDXS mapping at the interface between intact area and corroded area. Dashed curves in **(b)** and arrow in **(d)** show the electron-beam transparent film. Scale bars in **a, b, c, d,** and **e** indicate 1  $\mu\text{m}$ , 400 nm, 2  $\mu\text{m}$ , 500 nm, and 2  $\mu\text{m}$ , respectively.

hydrogen evolution rate (concomitant with a dynamic, time-dependent, passivation) which was  $\sim 4 \times 10^{-4}$ ,  $\sim 8 \times 10^{-4}$ , and  $\sim 5 \times 10^{-4} \text{ mL} \cdot \text{cm}^{-2} \cdot \text{h}^{-1}$  in 0.1 M, 0.6 M NaCl, and seawater, respectively, after 14 days immersion. This value is considerably lower than the most corrosion-resistant alloys ever reported, including Mg-0.3Ge<sup>23</sup>, BCC-Mg-Li-Al<sup>17</sup>, nanotwin-strengthened AZ80 alloy<sup>20</sup>. The hydrogen evolution rate of AM-AZ111 alloy is even lower than that of high-purity Mg, for which the hydrogen evolution after immersion for 2 weeks in 0.6 M NaCl with saturated Mg(OH)<sub>2</sub> ranged from 0.04–0.37 mL·cm<sup>-2</sup>·day<sup>-1</sup> (depending on the sample geometry)<sup>29</sup>. Fig. 2d reveals the mass-loss rate (0.06 mL·cm<sup>-2</sup>·day<sup>-1</sup>) and corrosion current of LPBF-AZ111 in 0.1 M NaCl, compared with pure Mg (highlighted by the dash lines) and other Mg alloys<sup>17,20,30–33</sup>. Measured under the same conditions, the corrosion current of AZ111 is ten times lower than the extruded AZ91<sup>32</sup>.

### Surface morphology after corrosion

The samples after immersion in 0.1 M and 0.6 M NaCl and seawater are shown in Supplementary Fig. 3. In seeking to observe some signs of corrosion, what appears to be a superficial surface staining form of corrosion was detected at the specimen edge, with the majority of bulk specimens visually pristine, which is not observed for Mg alloys after such an extended immersion time. The inspection by SEM of the bulk (near centre) region of the LPBF-AZ111 sample, following immersion, revealed a filiform-like corrosion morphology—that is commonly observed as the corrosion morphology for Mg-alloys in NaCl electrolytes. However, the area affected by filiform corrosion was limited over 14-days immersion. To understand why the evidence of superficial and filiform corrosion did not expand to the bulk of the sample, the corroded area at the edge of the sample was observed at higher magnification (Fig. 3). It was revealed that the intact part of the surface was fully covered by Mg(OH)<sub>2</sub> flakes (Fig. 3a). There was a high density of ultra-fine particles that had a similar size and morphology as the Mg<sub>17</sub>(Al, Zn)<sub>12</sub> particles in the bulk. Furthermore, it was generally observed that part of the Mg(OH)<sub>2</sub> flakes was covered by a cloud-like film, as highlighted in Fig. 3b. At the transition region between the corroded surface and intact surface, the fissures seemed to propagate toward the intact area (Fig. 3c).

However, at higher magnification, a surface film that is even electron transparent was observed to cover the lateral fissure-like tip (red arrow in Fig. 3d). Figure 3e–h reveals a higher Mg concentration in the intact area but higher oxygen and a lower Mg concentration in the apparently corroded area, indicating the accumulation of MgO/Mg(OH)<sub>2</sub> there.

### Surface film analysis

In order to further illustrate a rationale for the low corrosion current density in the as-polished state and during immersion, the LPBF-AZ111 surface before and after immersion in 0.1 M NaCl was analytically characterised using X-ray photoelectron spectroscopy (XPS). The concentration of metallic atoms and cations as a function of depth from the surface is presented (Figs. 4 and 5). Figure 4 indicates that for the LPBF-AZ111 surface exposed to air, there is no distinguishable film or layered structure, however, Al enrichment was observed. Starting from the outermost surface until 180 nm beneath the surface, the mole fraction of Mg<sup>2+</sup> decrease steadily from  $\sim 82\%$  to  $\sim 60\%$ , whilst the fraction of Mg<sup>0</sup> and Al<sup>0</sup> increase from  $\sim 5$  to  $\sim 23\%$ , and  $\sim 1.2\%$  to  $\sim 7.4\%$ , respectively. The fraction of Al<sup>3+</sup> decreased slightly from 11% to 9% (Fig. 4a). The Al/Mg ratio was about 0.14 at the outermost surface, which increased to 0.2 linearly up to 180 nm depth (Fig. 4b). Apparently, the Al enrichment still occurs, even without NaCl immersion and from atmospheric exposure. It was determined that the Al<sup>3+</sup>/Mg<sup>2+</sup> ratio increased slightly from  $\sim 13.5\%$  to  $\sim 15\%$  from the surface to 180 nm depth (Fig. 4c). The Al<sup>0</sup>/Mg<sup>0</sup> ratio is much higher and increased from 0.22 at the surface to 0.32 at 180 nm depth (Fig. 4d). Among all the metallic (Mg, Al, Zn, Mn) and non-metallic (O, C) elements, the O and C fractions decreased from 57% to 49% and from 12% to 4%, respectively (Fig. 4e). From the surface to 81 nm, the fraction of OH<sup>-</sup> group is more than that of the O<sup>2-</sup> group (Fig. 4f). Beneath 81 nm, the O<sup>2-</sup> group has a higher fraction. The enrichment of Al near the air-exposed surface may rationalise the low corrosion current density (2.6  $\mu\text{A}/\text{cm}^2$ ) of the polished sample.

For the surface of immersed sample, all metallic elements were in the form of cations up to 75 nm (Fig. 5a). Beyond 75 nm, the fraction of Mg<sup>2+</sup> and Al<sup>3+</sup> decreased whilst the fraction of Mg<sup>0</sup> and Al<sup>0</sup> increased. The ratio between Al and Mg was about 0.2 at

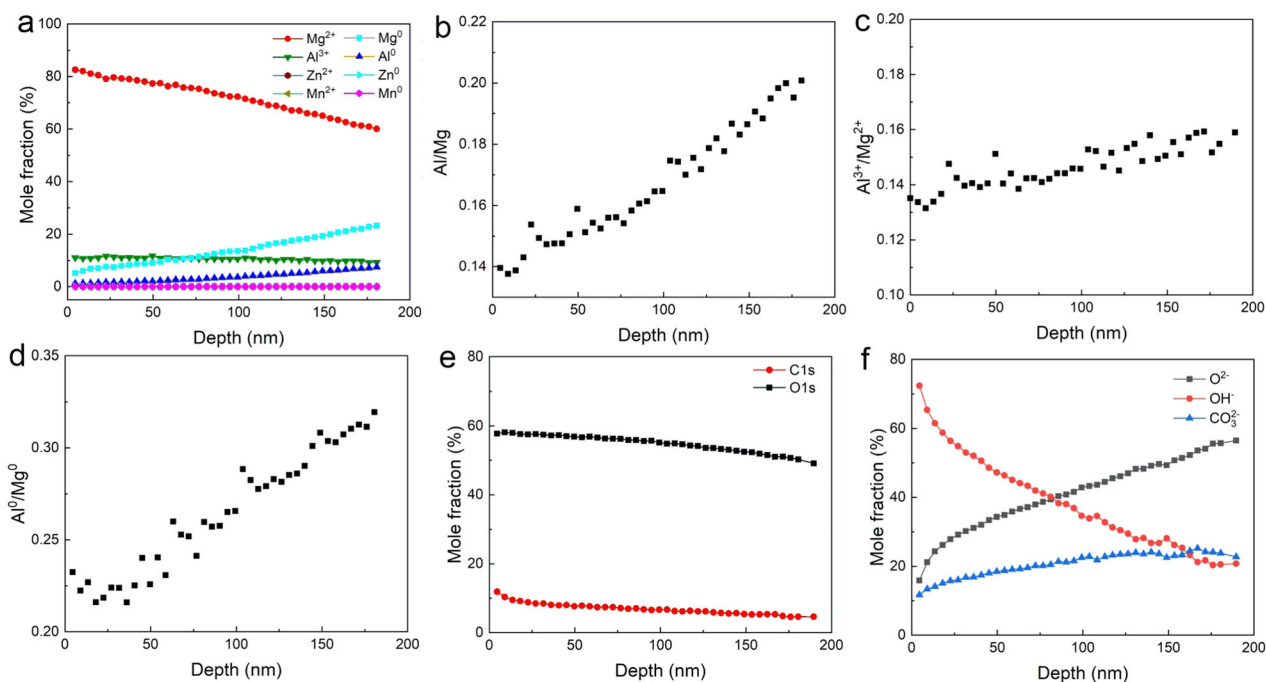


**Fig. 4** XPS analysis of elemental distribution of air-exposed surface. XPS measurements revealing (a) fraction of each cation and elemental metal, (b) Al/Mg ratio, (c)  $\text{Al}^{3+}/\text{Mg}^{2+}$  ratio, (d)  $\text{Al}^0/\text{Mg}^0$  ratio, (e) ratio fraction of O and C among metallic and non-metallic element, and (f) fraction among  $\text{O}^{2-}$ ,  $\text{OH}^-$ , and  $\text{CO}_3^{2-}$  ratio.

the outmost surface, which increased to 0.4 linearly up to 150 nm depth and then stabilised until  $\sim 364$  nm depth (Fig. 5b). The XPS results of  $\text{Al}^{3+}/\text{Mg}^{2+}$  ratio indicate three layers (Fig. 5b). In Layer 1 (0–75 nm), no  $\text{Al}^0$  and  $\text{Mg}^0$  were detected, and  $\text{Al}^{3+}/\text{Mg}^{2+}$  ratio was about 0.2. Layer 2 (75 nm–225 nm) seemed to be a transition layer, in which the  $\text{Al}^{3+}/\text{Mg}^{2+}$  ratio was increased from 0.2 to 0.3. In Layer 3 (225 nm–364 nm),  $\text{Al}^{3+}/\text{Mg}^{2+}$  ratio is highly scattered between 0.22–0.3. It is evident that the significance of Al enrichment near the immersed surface is much greater than for the scenario of the air-exposed surface (Fig. 4b, c).

The non-metallic elements O and C, were analysed (Fig. 5c, d). Among all the metallic (Mg, Al, Zn, Mn) and non-metallic (O, C) elements, the O and C fractions decreased from 55% to 33% and from 20% to 1%, respectively (Fig. 5c). Analysis of anion fraction also showed a 3-layer structure (Fig. 5d). Layer 1 (0–75 nm) was a hydroxide layer, in which the  $\text{OH}^-$  decreased and  $\text{O}^{2-}$  increased with the depth. Layer 2 (75–225 nm) was the oxide-rich layer. In Layers 1 and 2, the fraction of  $\text{CO}_3^{2-}$  was about 10%–15%, and became zero in the inner layer (Layer 3). In Layer 3, the  $\text{O}^{2-}$  fraction is  $<40\%$ ; O fraction  $<40\text{--}50\%$  is used as an indicator of bulk alloy substrate<sup>34–36</sup>. The fittings of Mg, Al, O, and C peaks of XPS spectrum at different depths were provided in Supplementary Figs. 4 and 5.

Based on the analysis of elemental atoms, it is evident that the surface film was dynamically formed during immersion, with a two-layered structure evolving in a time-dependent manner. The thickness of the film was  $\sim 225$  nm. In the out hydroxide-rich layer (0–75 nm), the fraction of  $\text{Al}_2\text{O}_3$  is about 15%–20%, whilst the  $\text{MgO}$ ,  $\text{MgCO}_3$  and  $\text{Mg}(\text{OH})_2$  in total is about 80%. In this layer, with the increasing depth, the fraction of  $\text{Mg}(\text{OH})_2$  decreased, but the fraction of  $\text{MgO}$  increased. In the inner oxide-rich transition layer (75 nm–225 nm), Mg-based compounds decreased significantly, but the fraction of  $\text{Al}_2\text{O}_3$  was nearly a constant at  $\sim 12\%$ . Beneath 225 nm was essentially bulk substrate, where the fraction of compounds in total decreased to  $\sim 30\%$ , and the fraction of elemental Mg and Al increased to 48% and 22%, respectively.

## DISCUSSION

The nature of the surface film, as depicted by Fig. 5, is unique. In previous studies<sup>20–22</sup>, Mg alloys through severe plastic deformation have also revealed observable passivation (albeit short-lived and not dynamically improving). In such cases, grain boundaries and twin boundaries were proposed to play a vital role in enhancing corrosion resistance by accelerating the formation of magnesium oxide and hydroxide surface bilayer<sup>20–22,37</sup>. Apart from grain refinement, the refinement of intermetallic phases, either by deformation<sup>38,39</sup> or laser surface melting<sup>40,41</sup>, also posited to lead to an apparently more uniform and shallow corrosion morphology. However, refinement itself is unlikely to be the dominant mechanism for the stark passivity observed in the polarisation curves herein. Indeed, the longer-term corrosion rate of extruded fine-grained Mg is only marginally lower than that of coarse-grained pure Mg, despite passivation observed in the polarisation curve of fine-grained pure Mg<sup>42</sup>. Moreover, if a stable passivation layer is formed, the EIS-determined Nyquist plot should reveal the characteristic of a positive  $-Z''(\omega)$  at lower frequency<sup>28</sup>. However, this ‘fingerprint’ of passivity has not been observed in ultra-fine-grained Mg alloys<sup>20–22</sup>, whilst very clear in this study (Fig. 2d). The outstanding corrosion resistance of AM-AZ111 is unlikely to be caused by merely increased Al concentration in the alloy. Several papers have reported the corrosion resistance and electrochemical behaviour of cast Mg alloy with 10–12 wt.% Al<sup>43,44</sup>. The hydrogen evolution of Mg-10Al(-0.3Mn) alloy is about  $6\text{--}8\text{ mL}\cdot\text{cm}^{-2}$  in  $72\text{ h}^{43}$ , which is substantially higher than that of AM-AZ111 alloy in this study ( $0.13\text{ mL}\cdot\text{cm}^{-2}$ ) in the same electrolyte (0.6 M or 3.5 wt.% NaCl solution). In 3 wt.% NaCl solution, the hydrogen evolution rate of Mg-11.6Al cast alloy is very high, about  $45\text{ mL}\cdot\text{cm}^{-2}\cdot\text{day}^{-144}$ , whilst that of AM-AZ111 is  $<0.7\text{ mL}\cdot\text{cm}^{-2}\cdot\text{day}^{-1}$  in Day 1 and then decreasing with an increase in immersion time. If the supersaturated Mg-Al is manufactured by physical vapour deposition, rather than casting, which also realises rapid cooling similar to LPBF, then the corrosion current  $i_{\text{corr}}$  of Mg-11Al alloy ( $2.2\ \mu\text{L}\cdot\text{cm}^{-2}$ ) is similar to the result of our study<sup>45</sup>. These observations from published

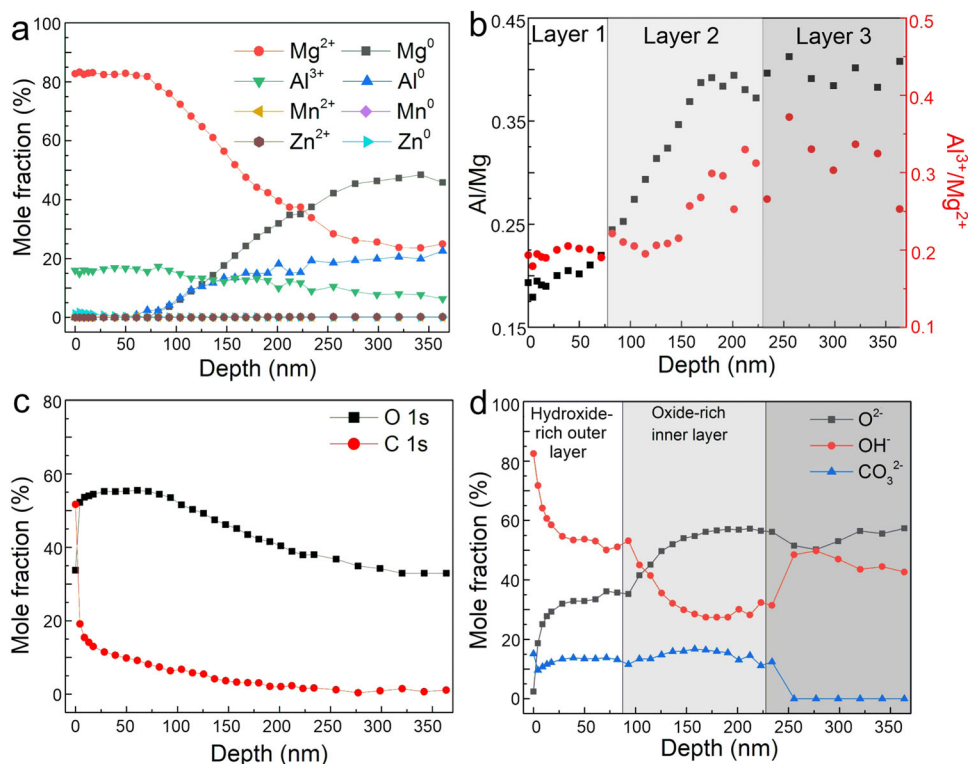


**Fig. 5** XPS analysis of elemental distribution of NaCl-immersed surface. **a** fraction of each cation and elemental metal, **b** Al/Mg and  $\text{Al}^{3+}/\text{Mg}^{2+}$  ratio, **c** fraction of O and C among metallic and non-metallic element, and **d** fraction among  $\text{O}^{2-}$ ,  $\text{OH}^-$ , and  $\text{CO}_3^{2-}$  ratio, as a function of depth.

papers support the claim that the enhanced corrosion resistance is caused by a combination of the LBPf-induced microstructure, phase composition along with the correct selection of alloy composition. In fact, for the cast Mg-Al alloys, the higher Al composition beyond 10 wt.% will substantially increase the degradation rate<sup>46</sup>.

Herein, we propose that rather than microstructural refinement, the elemental distribution at the near-surface dictates the occurrence of passivation and corrosion rate more than microstructural refinement. In the case herein, the development of a critical surface Al-concentration appears to be a dynamic and time-dependent process. A process that has not previously been reported in the cast or conventional Mg-alloys where the concentration of Al is notionally <9 wt. %. The mechanism is depicted in Fig. 6. Once immersed in the NaCl electrolyte (Fig. 6a), the corrosion mechanism of LPBF-AZ111 is similar to that of other Mg alloys initially. An incomplete MgO layer forms, and localised corrosion processes with local anodes and cathodes adjacent to the developing surface layers that include MgO and  $\text{Mg}(\text{OH})_2$ . At local anode sites,  $\text{Mg}^{2+}$  ions are released at a comparatively fast rate, reacting with water. The resultant  $\text{Mg}(\text{OH})_2$  deposits on the surface and MgO film, forming characteristic  $\text{Mg}(\text{OH})_2$  flakes. Under such circumstances, there is no passivation, and the temporal evolution of corrosion propagation with anodes and cathodes spatially developing—with oxide-hydroxide corrosion products having been shown to catalyse hydrogen evolution and accelerate corrosion<sup>47–49</sup>. However, with the increased duration for immersion, the dissolution rate of Mg (which is a necessary precursor or step required) decreased as the passivation film eventually formed due to critical Al surface enrichment (Fig. 6b). In the Al-rich substrate beneath the oxide layer, the mole fraction of  $\text{Al}^0$  among the elemental metals can be as high as 30% (Fig. 6c). Therefore, abundant Al atoms can diffuse into the oxide-rich layer and the hydroxide-rich layer, where the Al atoms react with  $\text{O}^{2-}$ .

Therefore, despite localised corrosion at the initial stage of immersion, an Al-rich passivation film and an Al-rich substrate beneath the film eventually formed, suppressing further Mg dissolution and hydrogen evolution.

To further support the claim of Al enrichment and its effectiveness on resisting corrosion, orthophosphoric acid ( $\text{H}_3\text{PO}_4$ ) solution was used to form a thicker surface layer in the immersion test. The oxide layer with the thickness <3  $\mu\text{m}$  was observed after 24 h immersion (Fig. 7a–c). The Al concentration in the oxide layer and adjacent substrate was much higher than that in the bulk. With the longer immersion time (72 h), the increment of oxide film thickness was marginal, <4  $\mu\text{m}$ , and without severe localised corrosion (Fig. 7d–f). The Al enrichment at the surface was more obvious, and the Al concentration at the oxide/substrate interface was notably higher (Fig. 7e). The observation suggested that the Al enrichment at the surface even significantly enhanced the durability in acid, whilst corrosion resistance of Mg in such an acidic environment was previously thought impossible. The capability of Al enrichment at the oxide/substrate interface of LPBF-AZ111 alloy should be primarily due to preferential dissolution of Mg, and the local near-surface environment that allows the development of the complex film articulated herein. Such a complex film structure is not likely to form in cases where the initial alloy concentration includes so much alloying as to prevent the dynamic passivation mechanism. It was reported that in Mg-Al binary alloys, the Mg dissolution is strongly selective at a high rate, and the rapid leaching of Mg leads to the formation of Al-rich surface<sup>50</sup>.

For the air-exposed surface, although there is not dissolution/leaching of elements, the enrichment of Al is also observed (even though less significant than the enrichment of immersed surface). More importantly,  $\text{Al}^{3+}/\text{Mg}^{2+}$  ratio is low, but  $\text{Al}^0/\text{Mg}^0$  ratio is much higher (Fig. 4d). It suggests that the enrichment is predominantly caused by Al atoms, rather than ions, close to

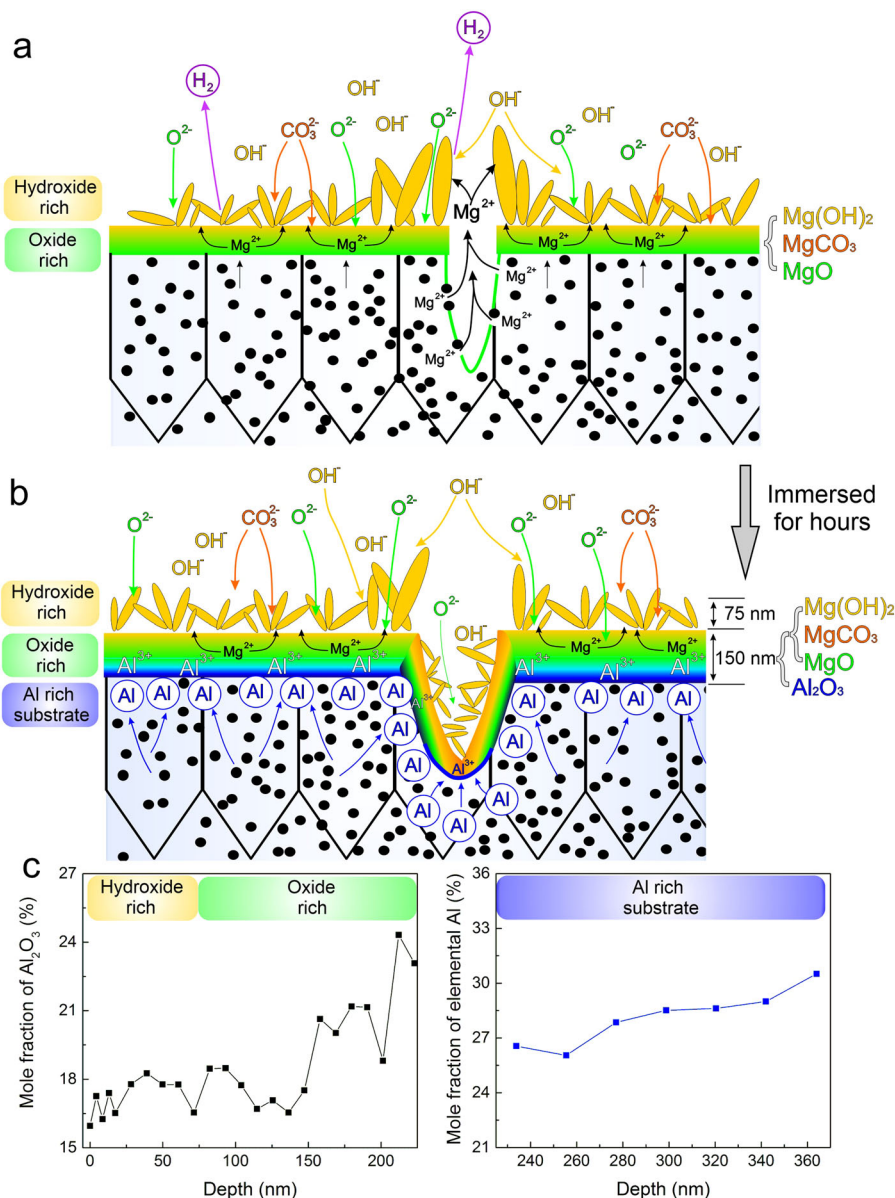


**Fig. 6 Structure of passivation film.** Schematic diagrams showing laser powder-bed fusion AZ111 alloy immersed in NaCl (**a**) at the initial stage and (**b**) after hours of immersion when passivation is developed. **c** XPS showing mole fraction of  $\text{Al}_2\text{O}_3$  among compounds in the hydroxide-rich and oxide-rich layers, and mole fraction of elemental Al among metallic elements in the Al-rich substrate.

the surface. Apart from diffusion, it is unlikely to have other mechanisms that can result in the significant increase in the Al atom concentration near the air-exposed surface. Thermodynamically, the major driving force for solute segregation to the surface is the decrease in surface free energy and lattice strain energy which accompanies the transfer of misfitting solute atoms from the lattice to the surface<sup>51</sup>. This process is affected by the solute atoms available to segregate, and the increasing solute supersaturation ( $C_b - C_{eq}$ , where  $C_b$  is the bulk solute content and  $C_{eq}$  is the equilibrium solute content) will also increase the driving force for such surface segregation, as demonstrated in Cu-Ti system<sup>52</sup>. In Mg-Al system, the equilibrium solute content of Al in Mg at room temperature does not exceed 1 wt.%<sup>1</sup>. In the matrix of AZ111 alloy, Al concentration is  $\sim 7.5\%$  (Fig. 1), much higher than that of the cast AZ91 alloy ( $\sim 2.5\%$ , Supplementary Fig. 6). This indicates that plenty of Al atoms are in the supersaturated state existing in the matrix of AZ111 alloy, which can only be achieved by rapid solidification ( $10^5$  to  $10^6 \cdot \text{K} \cdot \text{s}^{-1}$ ) associated with the LPBF<sup>3</sup>.

Moreover, a high level of micro-strain due to the rapid solidification may also provide the driving force to facilitate the atom diffusion to the sample surface. Fundamentally, the amount of residual stress will alter the free energy state of the material, which, in turn, can impact the corrosion kinetics and promote the formation of a passive layer in the passive system<sup>22</sup>. Kinetically, however, the Al diffusion rate is very slow even along grain boundaries at room temperature. Given grain boundary diffusion is faster, the diffusion of Al in Mg along grain boundary was calculated. The data was adopted from ref. <sup>53</sup>. The activation energy for GB diffusion equals that of lattice diffusion<sup>54</sup>. Using the equation  $D_{GB} = D_0 \exp(-Q_{GB}/RT)$ , where  $R$  is gas constant  $8.314 \text{ J} \cdot \text{mol}^{-1} \cdot \text{K}^{-1}$  and  $T$  is temperature (298 K), the calculated  $D_{GB}$  at room temperature is about  $1.7 \times 10^{-20} \cdot \text{cm}^2 \cdot \text{s}^{-1}$ . This value is low compared to the value required for surface layer as observed in this study, and thus the preferential dissolution of Mg in electrolyte may be the key reason for the Al enrichment at the NaCl-immersed surface.

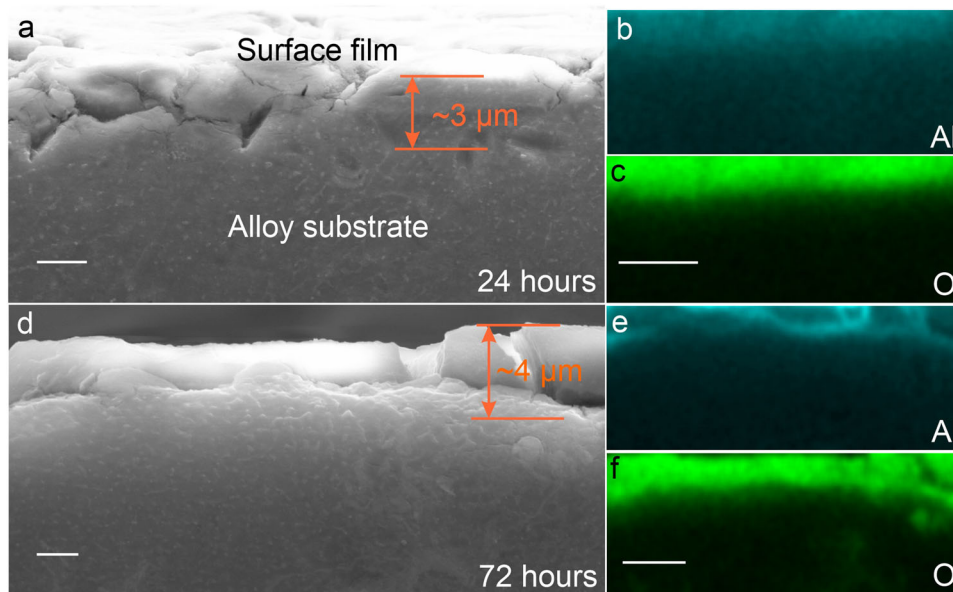


**Fig. 7 Aluminium enrichment at the surface after immersion in orthophosphoric acid solution (pH = 2.5).** SEM images and corresponding EDXS maps of Al and O elements after LPBF-AZ111 was immersed for (a–c) 24 and (d–f) 72 h. Scale bars in a and d indicate 2  $\mu\text{m}$ , and in b, c, e, f indicate 5  $\mu\text{m}$ .

**Table 1.** Composition of LPBF sample (in wt.%).

	Mg	Al	Zn	Mn	Fe	Cu	Ni	Si
LPBF sample	Bal.	10.6	0.54	0.28	0.004	0.002	0.003	0.02

In this study, we demonstrate that LPBF is capable of producing Mg alloys that show strong passivation and the lowest degradation rate ever known. Such outstanding electrochemical durability should be caused by the supersaturated Al solid solution and a high density of micro-strain that in combination allows Al to segregate to the surface and form an Al-rich layer. In addition to the outstanding durability, the LPBF-AZ111 alloy has high compressive yield strength of  $\sim 300$  MPa (Supplementary Fig. 7) and high Vicker's hardness of  $99 \pm 2.0$  HV parallel to the BD and  $100 \pm 3.5$  HV perpendicular to the BD. The findings of this study constitute an important step towards manufacturing super-lightweight alloys with outstanding corrosion resistance for high-value-added applications.

## METHODS

### Materials preparation

The bulk alloy was chill cast and subsequently pulverised by atomic gas atomisation. The powder was then sieved to obtain the following common particle size distribution necessary for the latter laser powder-bed fusion (LPBF): D10 34.8  $\mu\text{m}$ , D50 54.5  $\mu\text{m}$  and D90 88.4  $\mu\text{m}$  (Supplementary Fig. 8). Particle size distribution was calculated via laser diffraction (Mastersizer 3000, Malvern Panalytical, Malvern, UK). The microscopical screening of the manufactured powder revealed a highly spherical powder shape with few small satellite particles. Cuboid specimens were manufactured from the powder via LPBF, utilizing a modified laboratory-scale setup (AconityMINI, Aconity3D GmbH, Aachen, Germany) with a maximum laser power of 400 W (as previously reported)<sup>55</sup>. Specifically, a laser power of 50 W with a scanning speed of 400 mm/s, a hatching distance of 40  $\mu\text{m}$  and a layer thickness of 30  $\mu\text{m}$  was applied. The employed scan strategy was parallel lines with orthogonal orientation respective to the previous layer. A standard zig-zag laser exposure pattern with a scanning angle of 90° between adjacent layers was used, while the building plate consisted of pure Mg to assure optimal connection between the support structure and building plate. Manufacturing was always performed under an inert gas atmosphere (oxygen concentration below 200 ppm), utilizing Argon 5.0.

The composition of the LPBF sample was measured by inductively coupled plasma optical emission spectroscopy (Table 1).

### Electrochemical and immersion testing

Electrochemical measurements were performed with a three-electrodes flat cell (K-0235, Princeton Applied Research) with a Saturated Calomel Electrode (SCE) as the reference, and platinum mesh as the counter electrode. Test specimens (working electrode) were mounted in epoxy resin and ground (under ethanol) to a 2000 grit finish using SiC paper. All the electrochemical tests were carried out using 200 ml of 0.1 M NaCl (pH = 6.5–7). A Bio-Logic® VSP potentiostat was utilised for electrochemical testing. Potentiodynamic polarisation measurements were obtained using a scan rate of 1 mV·s<sup>-1</sup>. The Tafel-type fitting and determination of corrosion current density and corrosion potential were obtained by EC-lab® Software (Version 11.27). To obtain the  $i_{\text{corr}}$  value, a line was drawn on the potential axis, that intersects the measured  $E_{\text{corr}}$  value (this line is parallel to the current axis). The value of  $E_{\text{corr}}$  is readily discerned as a singular value of potential. Next, another line was drawn, which is a linear approximation to the cathodic polarisation curve, in the region of  $\sim -50$ – $-150$  mV from the  $E_{\text{corr}}$ . Where the two lines intersect, is a Tafel-type approximation of  $i_{\text{corr}}$ . Electrochemical impedance spectroscopy (EIS) was performed over the frequency range of 100 kHz to 10 mHz, with a polarising signal of 10 mV. All tests were carried out at least in triplicate.

For immersion testing, specimens were immersed in a 200 ml of quiescent 0.1 M and 0.6 M NaCl electrolyte (pH = 6.5) and seawater (pH = 8) for 14 days, and orthophosphoric acid solution (pH = 2.5) for 72 h, at room temperature (maintained at 23 °C). Seawater was obtained from Batemans Bay, Australia. Prior to immersion, the samples were ground to 4000 grit, then mirror polished with colloidal silica solution, sonicated in ethanol, air-dried and weighed with a calibrated balance with an accuracy of 0.01 mg. In order to combine the mass-loss experiment with the volumetric hydrogen collection in a single step, an inverted funnel was placed over the immersed sample and the evolved hydrogen was collected inside a burette. Before removing the corrosion products with a solution of 10% chromium trioxide (CrO<sub>3</sub>) + 1% silver nitrate (AgNO<sub>3</sub>) + 1% barium nitrate (Ba(NO<sub>3</sub>)<sub>2</sub>) for 60 s, the corrosion morphology was characterized using scanning electron microscopy.

### Scanning electron microscopy and transmission electron microscopy

Scanning electron microscopy (SEM) was performed using Zeiss UltraPlus equipped with Oxford Symmetry EBSD detector. EBSD was performed at 20 kV and 12 nA with a step size of 0.4  $\mu\text{m}$ . The samples for SEM and EBSD



characterisation are prepared by 4000-grit SiC sandpaper grinding, 50 nm colloidal silica suspension polishing, and ion polished by Leica TIC 3X Triple Ion Beam Cutter. The ion polish was operated at 8 kV and 3 mA for 6 min. The angle between the incident ion beam and sample surface was 7.5°. STEM and STEM-EDXS characterisation were performed using JOEL2100 operating at 200 kV. The samples were 3-mm diameter discs prepared by low-speed saw cutting, followed by mechanical grinding to a thickness of 50 µm using 4000 grid SiC paper. Samples were then ion-polished using a Gatan Precision Ion Polishing System (voltage 4.8 kV and angle 4°) at −100 °C, until a small hole formed in the specimen.

### X-ray photoelectron spectroscopy

X-ray photoelectron spectroscopy (XPS) was performed using a Thermo Scientific Nexsa Surface Analysis System calibrated to Au 4f and equipped with a hemispherical analyser. The incident radiation was monochromatic Al K $\alpha$  X-rays (1486.6 eV) at 72 W (6 mA and 12 kV, 400 × 800 µm<sup>2</sup> spot). Survey (wide) and high-resolution (narrow) scans were recorded at analyser pass energies of 150 eV and 50 eV and step sizes of 1.0 eV and 0.1 eV, respectively. The base pressure in the analysis chamber was <math>5.0 \times 10^{-9}</math> mbar. A low-energy dual-beam (ion and electron) flood gun was used to compensate for surface charging. Data processing was carried out using Avantage software (Version 5.9921) and the energy calibration was referenced to the main line of C1s at 284.8 eV.

### X-ray diffraction

X-ray diffraction (XRD) was performed using a high-resolution PANalytical X'Pert PRO MRD system using Cu-K $\alpha$  radiation ( $\lambda = 0.154$  nm) operating at 40 kV and 40 mA, with step size 0.01° from 20° to 80° in 2 $\theta$  angle. The XRD was calibrated using the National Institute of Standards and Technology standard reference material LaB<sub>6</sub>. The sample for XRD was mechanically ground to a 4000 grit finish using SiC paper and an area of 10 mm × 10 mm.

### Compression and hardness test

Compression test was performed in an Instron 4505 mechanical test machine. The sample was an as-built rod with a diameter of 7.5 mm and a height of 11 mm. The cross-head speed was 0.6 mm/min. The hardness test was performed on a Matsuzawa MHT-1 hardness tester with a load of 1 kgf. Seven indentations were performed for each test. The sample surface was ground using 4000 grit SiC sandpaper before indentation.

### DATA AND MATERIALS AVAILABILITY

The authors declare that the main data supporting the findings of this study are available within the article and its Supplementary Information files. Data is available from the corresponding author upon request.

Received: 15 November 2021; Accepted: 15 March 2022;

Published online: 20 April 2022

### REFERENCES

- Polmear, I., StJohn, D., Nie, J. F. & Qian, M. *Light Alloys* 5th edn (Butterworth-Heinemann, 2017).
- Nie, J. F., Shin, K. S. & Zeng, Z. R. Microstructure, deformation, and property of wrought magnesium alloys. *Metall. Mater. Trans. A* **51**, 6045–6109 (2020).
- DeRoy, T. et al. Additive manufacturing of metallic components—process, structure and properties. *Prog. Mater. Sci.* **92**, 112–224 (2018).
- Kurzynowski, T., Pawlak, A. & Smolina, I. The potential of SLM technology for processing magnesium alloys in aerospace industry. *Arch. Civ. Mech. Eng.* **20**, 23 (2020).
- Karunakaran, R., Ortgies, S., Tamayol, A., Bobaru, F. & Sealy, M. P. Additive manufacturing of magnesium alloys. *Bioact. Mater.* **5**, 44–54 (2020).
- Hyer, H. et al. Additive manufacturing of dense WE43 Mg alloy by laser powder bed fusion. *Addit. Manuf.* **33**, 101123 (2020).
- Li, Y. et al. Additively manufactured biodegradable porous magnesium. *Acta Biomater.* **67**, 378–392 (2018).
- Bär, F. et al. Laser additive manufacturing of biodegradable magnesium alloy WE43: a detailed microstructure analysis. *Acta Biomater.* **98**, 36–49 (2019).

- Gangireddy, S., Gwalani, B., Liu, K., Faierson, E. J. & Mishra, R. S. Microstructure and mechanical behavior of an additive manufactured (AM) WE43-Mg alloy. *Addit. Manuf.* **26**, 53–64 (2019).
- Wei, K., Gao, M., Wang, Z. & Zeng, X. Effect of energy input on formability, microstructure and mechanical properties of selective laser melted AZ91D magnesium alloy. *Mater. Sci. Eng. A* **611**, 212–222 (2014).
- Zhang, B., Liao, H. & Coddet, C. Effects of processing parameters on properties of selective laser melting Mg–9%Al powder mixture. *Mater. Des.* **34**, 753–758 (2012).
- Liu, S. et al. Influence of laser process parameters on the densification, microstructure, and mechanical properties of a selective laser melted AZ61 magnesium alloy. *J. Alloy. Compd.* **808**, 151160 (2019).
- Liu, C., Zhang, M. & Chen, C. Effect of laser processing parameters on porosity, microstructure and mechanical properties of porous Mg–Ca alloys produced by laser additive manufacturing. *Mater. Sci. Eng. A* **703**, 359–371 (2017).
- Wei, K., Wang, Z. & Zeng, X. Influence of element vaporization on formability, composition, microstructure, and mechanical performance of the selective laser melted Mg–Zn–Zr components. *Mater. Lett.* **156**, 187–190 (2015).
- Zumdick, N. A. et al. Additive manufactured WE43 magnesium: a comparative study of the microstructure and mechanical properties with those of powder extruded and as-cast WE43. *Mater. Charact.* **147**, 384–397 (2019).
- Nie, J. F. Precipitation and hardening in Magnesium alloys. *Metall. Mater. Trans. A* **43**, 3891–3939 (2012).
- Xu, W. et al. A high-specific-strength and corrosion-resistant magnesium alloy. *Nat. Mater.* **14**, 1229–1235 (2015).
- Kainer, K. U., Bala Srinivasan, P., Blawert, C., Dietzel, W. in *Non-Ferrous Metals and Alloys* (ed. Czerwinski, F) 2011–2041 (IntechOpen, 2010).
- Esmaily, M. et al. Fundamentals and advances in magnesium alloy corrosion. *Prog. Mater. Sci.* **89**, 92–193 (2017).
- Yan, C. et al. Evading strength–corrosion tradeoff in Mg alloys via dense ultrafine twins. *Nat. Commun.* **12**, 4616 (2021).
- Kim, H. S. & Kim, W. J. Enhanced corrosion resistance of ultrafine-grained AZ61 alloy containing very fine particles of Mg17Al12 phase. *Corros. Sci.* **75**, 228–238 (2013).
- Ralston, K. D., & Birbilis, N. Effect of grain size on corrosion: a review. *Corrosion* <https://doi.org/10.5006/1.3462912> (2010).
- Liu, R. L., Scully, J. R., Williams, G. & Birbilis, N. Reducing the corrosion rate of magnesium via microalloying additions of group 14 and 15 elements. *Electrochim. Acta* **260**, 184–195 (2018).
- Niu, X., Shen, H., Fu, J., Yan, J. & Wang, Y. Corrosion behaviour of laser powder bed fused bulk pure magnesium in hank's solution. *Corros. Sci.* **157**, 284–294 (2019).
- Esmaily, M. et al. A detailed microstructural and corrosion analysis of magnesium alloy WE43 manufactured by selective laser melting. *Addit. Manuf.* **35**, 101321 (2020).
- Gharbi, O. et al. On the corrosion of additively manufactured aluminium alloy AA2024 prepared by selective laser melting. *Corros. Sci.* **143**, 93–106 (2018).
- Choudhary, S., Cruz, V., Pandey, A., Thomas, S. & Birbilis, N. Element-resolved electrochemical analysis of the passivity of additively manufactured stainless steel 316L. *Corros. Sci.* **189**, 109576 (2021).
- Pedferri P. *Corrosion Science and Engineering* (Springer, 2018).
- Cao, F. et al. Corrosion of ultra-high-purity Mg in 3.5% NaCl solution saturated with Mg(OH)<sub>2</sub>. *Corros. Sci.* **75**, 78–99 (2013).
- Liu, R. L., Zeng, Z. R., Scully, J. R., Williams, G. & Birbilis, N. Simultaneously improving the corrosion resistance and strength of magnesium via low levels of Zn and Ge additions. *Corros. Sci.* **140**, 18–29 (2018).
- Xia, X. *The Effect of Composition on the Electrochemical Properties and Corrosion of Wrought Mg-Alloys*. PhD thesis, Monash Univ. (2017).
- Kateryna, G. *Development of Mg-Al-Zn Alloys With Enhanced Toughness and Durability*. PhD thesis, Monash Univ. (2017).
- Feng, J. et al. Unique corrosion resistance of ultrahigh pressure Mg–25Al binary alloys. *Corros. Sci.* **143**, 229–239 (2018).
- Mischler, S., Vogel, A., Mathieu, H. J. & Landolt, D. The chemical composition of the passive film on Fe–24Cr and Fe–24Cr–11Mo studied by AES, XPS and SIMS. *Corros. Sci.* **32**, 925–944 (1991).
- Jiang, R., Wang, Y., Wen, X., Chen, C. & Zhao, J. Effect of time on the characteristics of passive film formed on stainless steel. *Appl. Surf. Sci.* **412**, 214–222 (2017).
- Li, Y. et al. Early oxidation mechanism of austenitic stainless steel TP347H in supercritical water. *Corros. Sci.* **128**, 241–252 (2017).
- Ahmadkhaniha, D., Fedel, M., Heydarzadeh Sohi, M. & Deflorian, F. Corrosion behavior of severely plastic deformed magnesium based alloys: a review. *Surf. Eng. Appl.* **53**, 439–448 (2017).
- Jeong, Y. S. & Kim, W. J. Enhancement of mechanical properties and corrosion resistance of Mg–Ca alloys through microstructural refinement by indirect extrusion. *Corros. Sci.* **82**, 392–403 (2014).
- Gui, Z., Kang, Z. & Li, Y. Mechanical and corrosion properties of Mg–Gd–Zn–Zr–Mn biodegradable alloy by hot extrusion. *J. Alloy. Compd.* **685**, 222–230 (2016).

40. Abbas, G., Liu, Z. & Skeldon, P. Corrosion behaviour of laser-melted magnesium alloys. *Appl. Surf. Sci.* **247**, 347–353 (2005).
41. Guo, L. F., Yue, T. M. & Man, H. C. Excimer laser surface treatment of magnesium alloy WE43 for corrosion resistance improvement. *J. Mater. Sci.* **40**, 3531–3533 (2005).
42. op't Hoog, C., Birbilis, N. & Estrin, Y. Corrosion of pure Mg as a function of grain size and processing route. *Adv. Eng. Mater.* **10**, 579–582 (2008).
43. Li, X., Liu, S. & Du, Y. Investigation on the corrosion resistance of the Mg-10Al-xMn alloys based on thermodynamic calculations. *Corros. Sci.* **189**, 109631 (2021).
44. Liu, M. et al. Calculated phase diagrams and the corrosion of die-cast Mg–Al alloys. *Corros. Sci.* **51**, 602–619 (2009).
45. Wu, P. P., Song, G. L., Zhu, Y. X., Feng, Z. L. & Zheng, D. J. The corrosion of Al-supersaturated Mg matrix and the galvanic effect of secondary phase nanoparticles. *Corros. Sci.* **184**, 109410 (2021).
46. Xiao, D. H. et al. Effects of alloying elements on microstructure and properties of magnesium alloys for tripling ball. *Metall. Mater. Trans. A* **46**, 4793–4803 (2015).
47. Salleh, S. H., Thomas, S., Yuwono, J. A., Venkatesan, K. & Birbilis, N. Enhanced hydrogen evolution on Mg (OH)<sub>2</sub> covered Mg surfaces. *Electrochim. Acta* **161**, 144–152 (2015).
48. Curioni, M., Scenini, F., Monetta, T. & Bellucci, F. Correlation between electrochemical impedance measurements and corrosion rate of magnesium investigated by real-time hydrogen measurement and optical imaging. *Electrochim. Acta* **166**, 372–384 (2015).
49. Fajardo, S. & Frankel, G. S. Effect of impurities on the enhanced catalytic activity for hydrogen evolution in high purity magnesium. *Electrochim. Acta* **165**, 255–267 (2015).
50. Volovitch, P., Serdechnova, M. & Ogle, K. Aqueous corrosion of Mg–Al binary alloys: roles of Al and Mg. *Corrosion* **68**, 557–570 (2012).
51. Wynblatt, P. & Ku, R. C. Surface energy and solute strain energy effects in surface segregation. *Surf. Sci.* **65**, 511–531 (1977).
52. Tsukimoto, S., Morita, T., Moriyama, M., Ito, K. & Murakami, M. Formation of Ti diffusion barrier layers in thin Cu(Ti) alloy films. *J. Elec. Mater.* **34**, 592–599 (2005).
53. Zhou, B. C., Shang, S. L., Wang, Y. & Liu, Z.-K. Diffusion coefficients of alloying elements in dilute Mg alloys: a comprehensive first-principles study. *Acta Mater.* **103**, 573–586 (2016).
54. Robson, J. D. Effect of rare-earth additions on the texture of wrought magnesium alloys: the role of grain boundary segregation. *Metall. Mater. Trans. A* **45**, 3205–3212 (2014).
55. Benn, F. et al. Influence of surface condition on the degradation behaviour and biocompatibility of additively manufactured WE43. *Mater. Sci. Eng. C* **124**, 112016 (2021).

## ACKNOWLEDGEMENTS

The authors are grateful for financial support from the Australian National University (ANU) Futures Scheme, and Swedish Research Council and the Royal Swedish Academy of Engineering Sciences. We acknowledge the use of facilities at the ANU Centre for Advanced Microscopy, Nodes of Microscopy Australia, and Monash X-ray

Platform. Z. Z. acknowledges the assistance from Dr Felipe Kremer and helpful discussion with Dr. Yuman Zhu and Prof. Aijun Huang. S. C. acknowledges Monash Postgraduate Scholarship.

## AUTHOR CONTRIBUTIONS

Z.Z. designed the experiments, analysed experimental results, and drafted the manuscript. S.C. and Y.H. performed XPS. M.E., A.A., Z.Z., and N.B. designed the alloy and contributed to the alloy manufacturing. F.B., T.D., A.K. performed the laser powder-bed fusion of alloy. N.B. contributed to the experimental design, electrochemical tests and analysis, and manuscript preparation.

## COMPETING INTERESTS

The authors declare no competing interests.

## ADDITIONAL INFORMATION

**Supplementary information** The online version contains supplementary material available at <https://doi.org/10.1038/s41529-022-00241-5>.

**Correspondence** and requests for materials should be addressed to Zhuoran Zeng or Nick Birbilis.

**Reprints and permission information** is available at <http://www.nature.com/reprints>

**Publisher's note** Springer Nature remains neutral with regard to jurisdictional claims in published maps and institutional affiliations.



**Open Access** This article is licensed under a Creative Commons Attribution 4.0 International License, which permits use, sharing, adaptation, distribution and reproduction in any medium or format, as long as you give appropriate credit to the original author(s) and the source, provide a link to the Creative Commons license, and indicate if changes were made. The images or other third party material in this article are included in the article's Creative Commons license, unless indicated otherwise in a credit line to the material. If material is not included in the article's Creative Commons license and your intended use is not permitted by statutory regulation or exceeds the permitted use, you will need to obtain permission directly from the copyright holder. To view a copy of this license, visit <http://creativecommons.org/licenses/by/4.0/>.

© The Author(s) 2022